

## IONIZATION FRONT INSTABILITIES IN PRIMORDIAL H II REGIONS

DANIEL WHALEN<sup>1</sup> & MICHAEL L. NORMAN<sup>2</sup>*Draft version February 1, 2008*

## ABSTRACT

Radiative cooling by metals in shocked gas mediates the formation of ionization front instabilities in the galaxy today that are responsible for a variety of phenomena in the interstellar medium, from the morphologies of nebulae to triggered star formation in molecular clouds. An important question in early reionization and chemical enrichment of the intergalactic medium is whether such instabilities arose in the H II regions of the first stars and primeval galaxies, which were devoid of metals. We present three-dimensional numerical simulations that reveal both shadow and thin-shell instabilities readily formed in primordial gas. We find that the hard UV spectra of Population III stars broadened primordial ionization fronts, causing H<sub>2</sub> formation capable of inciting violent thin-shell instabilities in D-type fronts, even in the presence of intense Lyman-Werner flux. The high post-front gas temperatures associated with He ionization sustained and exacerbated shadow instabilities, unaided by molecular hydrogen cooling. Our models indicate that metals eclipsed H<sub>2</sub> cooling in I-front instabilities at modest concentrations, from  $1 \times 10^{-3}$  -  $1 \times 10^{-2} Z_{\odot}$ . We conclude that ionization front instabilities were prominent in the H II regions of the first stars and galaxies, influencing the escape of ionizing radiation and metals into the early universe.

*Subject headings:* H II regions: simulation—cosmology: theory—early universe

## 1. INTRODUCTION

Instabilities of several varieties are known to form in ionization fronts (I-fronts) in the galaxy today, giving rise to structures like elephant trunks and bright rims in star-forming regions of the interstellar medium (ISM). Two prominent types are shadow instabilities (Williams 1999) and thin-shell instabilities (Garcia-Segura & Franco 1996), which usually manifest as fingers of ionized gas protruding ahead of the front. Shadow instabilities form when a density fluctuation is advected through an R-type front, creating a dimple that first elongates but then stabilizes. When the front becomes D-type, the dimple can erupt in a jet if the shocked gas radiatively cools and forms a cold dense shell liable to fragmentation. Radiation escapes through fissures in the shell, causing the dimple to fracture and jet forward. Thin-shell instabilities arise when a D-type front encounters a density perturbation. If the prefront shocked gas efficiently cools, the perturbation triggers a Vishniac instability (Vishniac 1983) in the shell; if not, the shell may instead fracture due to Rayleigh-Taylor instabilities (Mac Low & Norman 1993). Either way, radiation rapidly destabilizes the perturbations by escaping through cracks in the shell and driving ionized extensions of gas much larger than the original disturbance into the surrounding medium. In a previous paper, we examined the topology of both types of instabilities in the ISM (Whalen & Norman 2007), confirming that their violence was determined by the cooling efficiency of the shocked gas.

H II regions appeared at the redshifts of first structure formation (Whalen *et al.* 2004; Kitayama *et al.* 2004), beginning with the formation of isolated mas-

sive stars in the first dark matter halos of mass  $\gtrsim 1.0 \times 10^5 M_{\odot}$  at  $z \sim 20 - 30$  (Abel *et al.* 2000, 2002; Bromm *et al.* 1999; Bromm *et al.* 2002) and continuing with the rise of the first stellar populations in primeval galaxies a few hundred Myr later. Whether I-front instabilities could form in pristine H and He at high redshifts is a key question in early cosmological reionization and structure formation for several reasons. First, they may have regulated UV escape from the first stars and galaxies, which has risen sharply in importance with the recent discovery of substantial free electron optical depths at by the *Wilkinson Microwave Anisotropy Probe* (WMAP) (Spergel *et al.* 2003; Kogut *et al.* 2003; Page *et al.* 2006), implying that cosmological reionization began much earlier than previously expected. Second, I-front instabilities may have created density condensations prone to clumping and later collapse, forming new generations of stars. Third, the mixing of metals from the first supernovae with remnants of I-front instabilities in relic H II regions determined the extent to which the early intergalactic medium (IGM) was chemically enriched. Contamination of instability relics may fracture and collapse them on mass scales very different from the stars that created them Mackey *et al.* (2003); Yoshida *et al.* (2007), abruptly splitting the primordial initial mass function (IMF) into a low-mass branch in just one generation. On the other hand, if saturated I-front instabilities drive turbulent flows, they may have supported clouds in minihalos or protogalaxies from collapse, postponing rather than promoting star formation (Whalen & Norman 2007). Finally, recent work by Mizuta *et al.* (2005, 2006) suggests that ionization fronts penetrating molecular cloud cores in the ISM may develop unstable modes that reach the centers of the core before the front. This may disrupt collapse of cloud cores into new stars, both in the galaxy and at high redshifts.

Given the central role of radiative cooling in modulating I-front instabilities in the ISM, one might question

<sup>1</sup> Applied Physics (X-2), Los Alamos National Laboratory

<sup>2</sup> Center for Astrophysics and Space Sciences, University of California at San Diego, La Jolla, CA 92093, U.S.A. Email: dwhalen@cosmos.ucsd.edu

whether they arose at all in primordial ionized flows, in which the atomic or molecular hydrogen cooling is far less efficient. Cosmological ionization fronts also differed from their galactic counterparts in being driven by the hard UV and soft X-ray spectra of Pop III stars and miniquasars. Such spectra exhibit a range of photon mean free paths that can, depending on the ambient density, greatly broaden the front, in some cases to as much as the Hubble distance. It is unclear what impact the broadening of the front would have on the formation and evolution of unstable modes in I-fronts; the temperature precursor preceding such fronts may preempt their formation entirely.

We have performed three-dimensional radiation hydrodynamical calculations of ionization front instabilities in which multifrequency radiative transfer is coupled to nine species primordial chemistry. We explore the formation of thin-shell and shadow instabilities in both primordial and incrementally-enriched gas in idealized geometries to disentangle their evolution from other features imprinted on the front by density inhomogeneities in real cosmological objects. As primordial fronts exit minihalos and protogalaxies they will encounter structures on several spatial scales that shape the global morphology of the final H II region (e.g., Abel et al. (2006)). For example, halos hosting Population III (Pop III) star formation exhibit filamentary inflows and other departures from sphericity on 100 pc scales (Abel *et al.* 2000; Fuller & Couchman 2000; Yoshida, Abel, Hernquist, & Sugiyama 2003). However, protostellar infall likely settles into an accretion disk on 1000 AU scales, collimating the emergent front into biconical flows above and below the plane of the disk (Tan & McKee 2004). Transverse gas velocities inherited from the angular momentum of the parent dark matter halo further complicate breakout of the nascent front on intermediate scales. We survey the formation of instabilities in primordial fronts in advance of multiscale simulations of UV breakout from primeval stars and galaxies.

In § 2 we describe the multifrequency upgrades to our photon-conserving radiative transfer in the ZEUS-MP reactive flow physics code documented in Whalen & Norman (2006). Primordial cooling processes are examined in § 3, particularly the role of H<sub>2</sub> cooling in cosmological ionization fronts. In § 4 we present our numerical models of D-type I-front instabilities due to thin-shell modes with atomic and molecular cooling. We follow the evolution of shadow instabilities associated with Pop III blackbody spectra in § 5, pinpoint the threshold at which metal line cooling triggers thin-shell instabilities in D-type fronts in § 6, and conclude in § 7.

## 2. RADIATIVE TRANSFER: CONSERVATIVE MULTIFREQUENCY PHOTON TRANSPORT

The monoenergetic radiative transfer in our previous studies does not capture postfront gas temperatures from first principles or the natural broadening of fronts by hard UV photons. It also neglects molecular hydrogen dissociation by Lyman-Werner photons and photodetachment of H<sup>-</sup>, key processes that regulate the abundance of H<sub>2</sub>, an important coolant in primordial gas. Here we describe modifications to our numerical method (Whalen & Norman 2006) for computing radiative rate

coefficients with a multifrequency algorithm that preserves photon conservation.

Constraining the number of absorptions in a zone due to all processes to equal the number of photons entering the cell minus those exiting leads to

$$n_{abs} \propto 1 - e^{-\tau}, \quad (1)$$

where

$$\tau = \sum_{i=1}^n \sigma_i n_i \Delta r, \quad (2)$$

is the total optical depth of the cell (the sum is over all removal processes). Equations 1 and 2 are true for a single energy and therefore hold if summed over all energies. The total absorption rates  $n_{abs}$  are necessary to determine the flux that reaches the next zone. On the other hand, the rate for a single removal process is a function of an attenuation factor that does not involve any of the other types of absorptions:

$$n_i \propto 1 - e^{-\tau_i}, \quad (3)$$

where  $\tau_i = n_i \sigma_i \Delta r$ , the optical depth to that interaction.

The sum of the individual rates evaluated in this manner is inconsistent with  $n_{abs}$ , but the two can be reconciled by enforcing

$$n_i \propto \frac{1 - e^{-\tau_i}}{\sum_{i=1}^n 1 - e^{-\tau_i}} n_{abs}. \quad (4)$$

This formulation guarantees that the sum of the rates matches the total rate associated with the optical depth of the zone (thus preserving photon conservation) while properly binning individual reactions according to their numbers. We evaluate rate coefficients (where  $k_i = n_i / (n V_{cell})$ , where  $n$  is the gas number density) at every frequency, assuming the photon emission rate  $\dot{n}(\nu_i)$  at that frequency, and sum them to obtain the total coefficient for the entire spectrum. We increment energy release in the gas one frequency at a time for a given photoreaction as well. In tests spanning 40 to 2000 logarithmically-spaced bins with a  $1 \times 10^5$  K Pop III blackbody spectrum, we obtain good convergence with 80 bins above the ionization limit of H.

We partition the emission rate  $\dot{n}_\gamma$  of ionizing photons of a Pop III star above from Schaerer (2002) into frequency intervals according to the number rate of a blackbody:

$$\dot{n}_\gamma = \sum_{i=1}^n \dot{n}(\nu_i) \Delta \nu \propto \sum_{i=1}^n \frac{(\nu_i/c)^2}{e^{h\nu_i/kT} - 1} \Delta \nu, \quad (5)$$

where the sum is over  $h\nu > 13.6$  eV. The emission rate for a particular bin is then

$$\dot{n}_{\gamma,j} = \dot{n}(\nu_j) \Delta \nu = \frac{\frac{(\nu_j/c)^2}{e^{h\nu_j/kT} - 1}}{\sum_{i=1}^n \frac{(\nu_i/c)^2}{e^{h\nu_i/kT} - 1}} \dot{n}_\gamma. \quad (6)$$

The procedure is similar for a quasar power-law flux spectrum  $F(\nu) d\nu \propto \nu^{-\alpha} d\nu$ . If  $\dot{n}_{QSO}$  is the ionizing emission

TABLE 1  
ZEUS-MP RADIATIVE REACTION PROCESSES

Rate	Reaction	Energy
k <sub>24</sub>	$H + \gamma \rightarrow H^+ + e^-$	$h\nu > 13.6 \text{ eV}$
k <sub>26</sub>	$He^+ + \gamma \rightarrow He^{++} + e^-$	$h\nu > 54.4 \text{ eV}$
k <sub>25</sub>	$He + \gamma \rightarrow He^+ + e^-$	$h\nu > 24.6 \text{ eV}$
k <sub>27</sub>	$H^- + \gamma \rightarrow H + e^-$	$h\nu > 0.755 \text{ eV}$
k <sub>28</sub>	$H_2^+ + \gamma \rightarrow H^+ + H$	$2.65 \text{ eV} < h\nu < 21 \text{ eV}$
k <sub>29</sub>	$H_2 + \gamma \rightarrow H_2^+ + e^-$	$h\nu > 15.42 \text{ eV}$
k <sub>30</sub>	$H_2^+ + \gamma \rightarrow 2H^+ + e^-$	$30 \text{ eV} < h\nu < 70 \text{ eV}$
k <sub>31</sub>	$H_2 + \gamma \rightarrow 2H$	$11.18 \text{ eV} < h\nu < 13.6 \text{ eV}$

rate for the quasar, a simple integration over frequency yields

$$\dot{n}(\nu) = \dot{n}_{QSO} \frac{\nu_{th}^\alpha \alpha}{\nu^{\alpha+1}} \quad (7)$$

from which follows

$$\dot{n}_{\gamma,j} = \dot{n}_{QSO} \left\{ \sum_{i=1}^n \frac{\nu_j^{\alpha+1}}{\nu_i^{\alpha+1}} \right\}^{-1} \quad (8)$$

We truncate the ionizing UV spectrum at 90 eV for Pop III stars.

The radiative processes now in the code are listed in Table 1. We adopted cross sections from Osterbrock (1989) to calculate k<sub>24</sub> and k<sub>26</sub>, from Abel et al. (1997) to compute k<sub>27</sub> and from Shapiro & Kang (1987) to evaluate k<sub>25</sub>, k<sub>28</sub>, k<sub>29</sub>, and k<sub>30</sub>. The rate coefficients k<sub>27</sub> and k<sub>28</sub> both extend below 13.6 eV; we allocate an additional 40 bins equally spaced between 0.755 eV and 13.6 eV to evaluate them. We obtain binned source rates over this energy range by constructing blackbody number spectra, normalizing them by total stellar luminosities taken from Schaerer (2002) instead of by total ionizing photon emission rates as before. Considerable speedups of the radiative transfer ( $\sim 30\%$ ) can be realized if the linear approximations to equations 1 and 3 are adopted in the limit of small optical depths, which are common for species like  $H^-$  and  $H_2^+$ . The k<sub>31</sub> calculation is decoupled from the radiative transfer and computed using the  $H_2$  self-shielding functions of Draine & Bertoldi (1996) corrected for thermal Doppler broadening (see also Abel et al. (1997))

$$k_{31} = 1.1 \times 10^8 \bar{F}(\nu) F_{shield}, \quad (9)$$

where  $F_{shield}$  is obtained from eq.37 of Draine & Bertoldi (1996) and  $\bar{F}(\nu)$  is the specific flux in  $s^{-1} \text{ ergs cm}^{-2} \text{ Hz}^{-1}$

$$\bar{F}(\nu) = \frac{1}{\Delta\nu} \int F(\nu) d\nu \quad (10)$$

and the frequency range corresponds to the Lyman-Werner band 11.18 eV to 13.6 eV. Total stellar luminosities are applied to derive  $F(\nu)$  for the blackbody spectrum. To approximate the effect of gas motion we assign a temperature of 10,000 K to the Doppler correction to the shielding function, as in Ahn & Shapiro (2007). The viability of thermal broadening as a proxy for flows in I-fronts is uncertain, but including it reduces shielding at intermediate column densities, setting lower limits on  $H_2$  cooling in the gas.

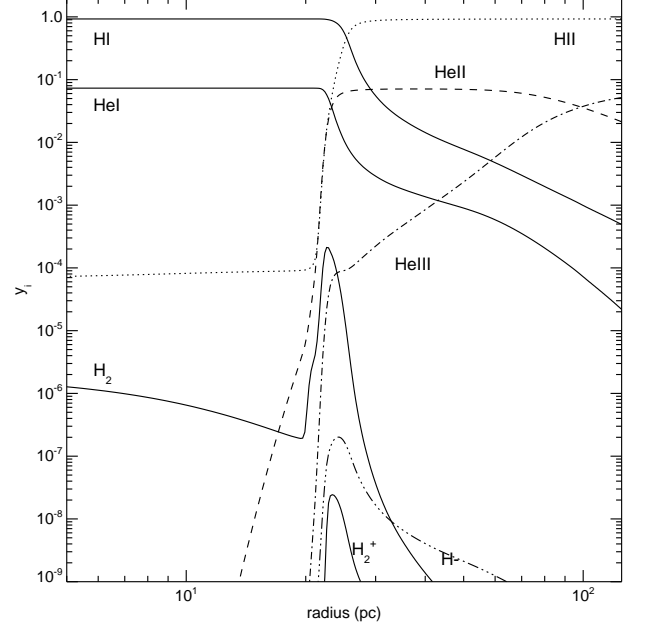
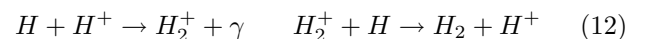
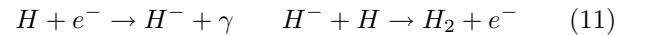


FIG. 1.— Primordial H and He abundances in a cosmological ionization front at  $t = 0.6t_*$ . In this figure, the radiation wave approaches from the right toward the halo centered at the left boundary. Compare to Fig. 8 of Ahn & Shapiro (2007) and the mirror image of Fig. 3 of Ricotti et al. (2001). Each curve is labeled by its species.

To test the coupling of the multifrequency transport to the nine-species reaction network (Anninos *et al.* 1997), we simulated the photoevaporation of a cosmological minihalo 540 pc from a 120  $M_\odot$  Pop III star. A spherically-symmetric truncated isothermal sphere (TIS) density profile was centered at the left  $x$  face of a 125 pc cartesian box with a uniform mesh of 512 zones. A geometrically attenuated plane wave propagated along the negative  $x$ -axis, engulfing the halo. This is the test case shown in Fig. 8 of Ahn & Shapiro (2007), and we adopted identical initial conditions for comparison to their one-dimensional lagrangian radiation hydrocode. Number fraction abundances for the primordial H and He species appear in Fig. 1 at  $0.6t_*$ , where  $t_*$  is the lifetime of the star.

Perhaps the most striking feature is the shell of molecular hydrogen created in the partially ionized outer layers of the front (Ricotti et al. 2001) (notice its peak coincides with an  $H$  II fraction  $\sim 0.1$ ). The hard UV photons in the spectrum transit a range of mean free paths in the neutral gas, broadening the front to approximately 5 pc. Free electron abundances at temperatures of a few thousand K in the finite width of the front rapidly catalyze  $H_2$  production by the  $H^-$  and  $H_2^+$  channels:



The peak  $H^-$  and  $H_2^+$  abundances are in step with the  $H_2$  peak, as expected since they are the key intermediaries for molecular hydrogen production in these relatively low densities. The  $H^-$  channel is dominant because

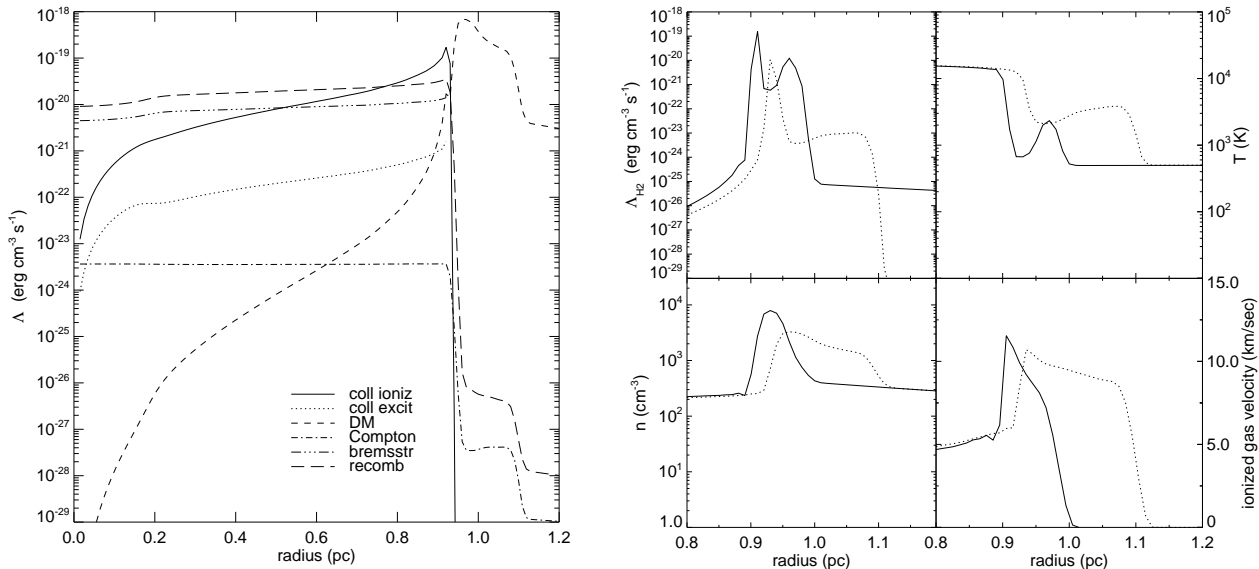


FIG. 2.— Left: Primordial cooling rates in the ionized gas and neutral shocked shell of an I-front at 100 Kyr not cooled by  $H_2$ . Dalgarno & McCray cooling rates, included for comparison, dwarf atomic H radiative rates in the dense shell. Right:  $H_2$  cooling rate, density, temperature, and velocity profiles for a primordial ionization front with no Lyman-Werner photodissociation (solid) and Lyman-Werner photodissociation (dotted).

it is more abundant and it has much higher  $H_2$  formation rates in these regimes. Fig. 1 is in good agreement with Fig. 8 of Ahn & Shapiro (2007) and is similar to Fig. 3 of Ricotti et al. (2001), which depicts H and He abundances for a primordial ionization front in a static uniform medium at the mean cosmological density (their figure should be compared to the mirror image of ours because their front propagates to the right). We note the relative abundances of  $H^-$  and  $H_2^+$  to be a general feature of partially ionized primordial gas at a few thousand K at these densities (compare Fig. 3 in Anninos *et al.* (1997), which features collisionally ionized gas collapsing in a pancake shock).

### 3. SHOCK COOLING IN PRIMORDIAL GAS

Five mechanisms that cool primordial H and He in I-front shocks are electron collisional and ionizational cooling, recombinational cooling, bremsstrahlung, and Compton cooling (primarily in the early universe). The free electrons required for these processes are present in minute quantities ( $n_e/n_H \sim 1 \times 10^{-4}$ ) at high redshifts and are either remnants of the recombination era or created in cosmological shocks. These channels cool H and He far less efficiently than metal lines in the ISM at  $T \lesssim 5000$  K. However, as discussed in § 2, molecular hydrogen may form in the I-fronts of very massive Pop III stars (Ricotti et al. 2001) and significantly raise cooling rates in the neutral gas.  $H_2$  ro-vibrational lines cannot rival metal cooling (since they can only lower primordial gas to  $\sim 200$  K instead of 10 - 20 K for metals) but are much more effective than H and He alone at temperatures below 5000 K.  $H_2$  formation is greatest in the partially ionized gas at the base of the shocked shell where energy losses may collapse the shell and trigger dynamical perturbations. However, the role of  $H_2$  cooling in primordial I-front instabilities is unclear because massive stars with strong ionizing luminosities are also intense sources of Lyman-Werner (LW) photons that dissociate  $H_2$ . With energies below the ionization limit, these photons can

cross the front and degrade the molecular hydrogen catalyzed in its outer layers.

We formulated three sets of one-dimensional calculations to examine I-front shocks when H, He and  $H_2$  cooling are present and absent. Collapse of the shell in one dimension is a rough predictor of instability formation in three dimensions. The initial density profile was:

$$n(r) = \begin{cases} n_c & \text{if } r \leq r_c \\ n_c(r/r_c)^{-2} & \text{if } r \geq r_c \end{cases}$$

with  $n_c$  and  $r_c$  equal to  $1 \times 10^4 \text{ cm}^{-3}$  and 0.2 pc, respectively.

A UV source with  $\dot{n}_{ph} = 1.0 \times 10^{48} \text{ s}^{-1}$  was centered in the mesh, ensuring the front would become D-type within the core. The grid was discretized into 200 uniform radial zones with inner and outer boundaries of 0.01 pc and 2.0 pc and reflecting and outflow boundary conditions, respectively. The gas was set to 500 K, appropriate to star-forming minihalos cooled by molecular hydrogen at  $z \sim 20$  (Abel *et al.* 2000, 2002). We chose a cooling cutoff (defined to be the gas temperature below which cooling curves were not applied to gas energy updates) equal to the cosmic microwave background  $T_{CMB} = 2.73(1+z)$  K with  $z = 20$ .

All three runs were multifrequency, with black-body spectra and nine-species primordial gas chemistry (Anninos *et al.* 1997). The gas profile was initialized with H and He number densities whose sum was equal to  $n_c$  but 76% and 24% H and He by mass, respectively. We adopted initial electron and  $H_2$  number fractions of  $1 \times 10^{-4}$  and  $2 \times 10^{-6}$  consistent with  $z \sim 20$  (Ricotti et al. 2001). When  $H_2$  cooling was included, the curves of Galli & Palla (1998) were utilized. The ionizing photon emission rate corresponds approximately to a star with a surface temperature, mass, and luminosity of 57,000 K,  $15 M_\odot$  and  $2.1 \times 10^4 L_\odot$  (Schaerer 2002), respectively. We applied these parameters to normalize the photon rates binned in each frequency interval.

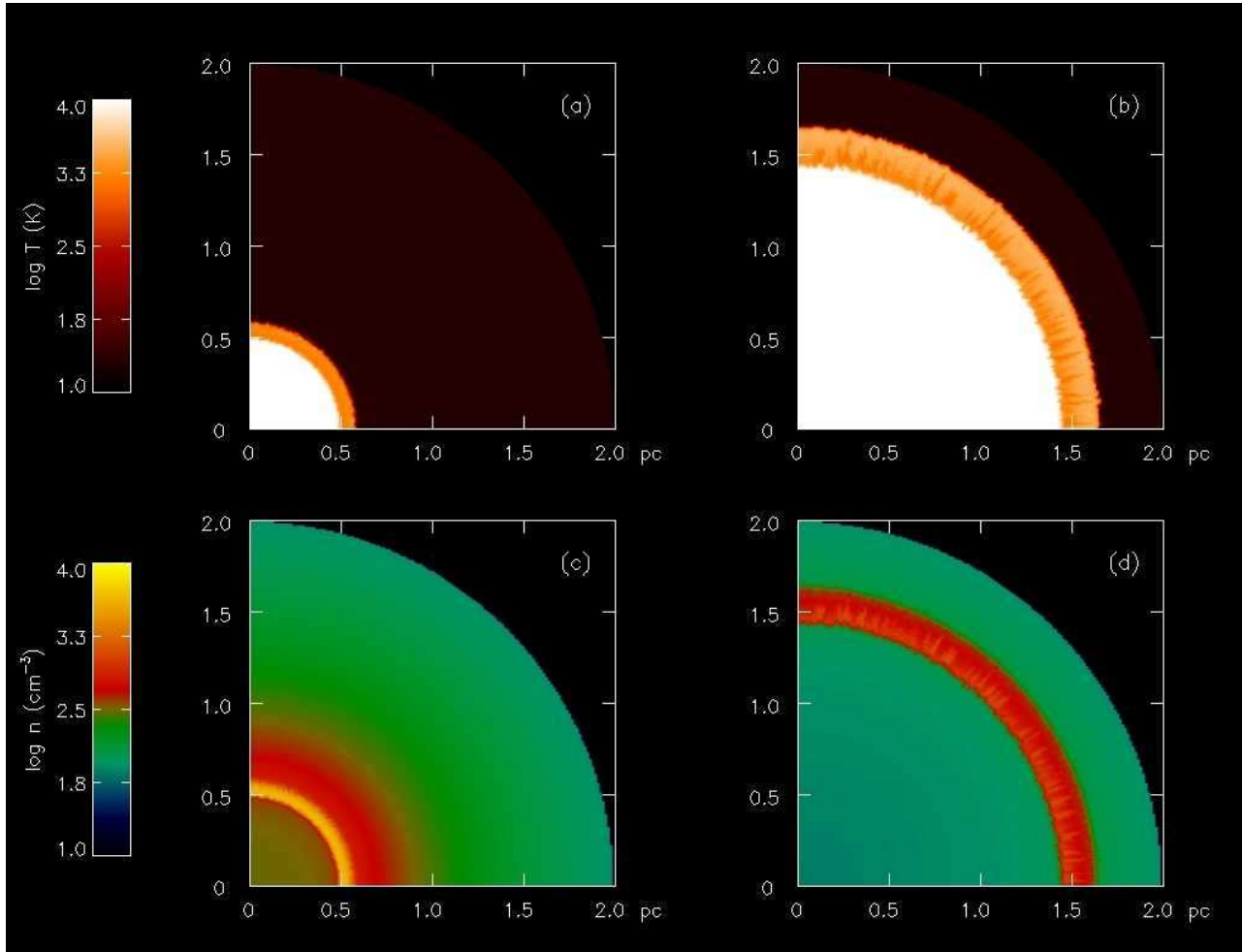


FIG. 3.— Evolution of a D-type front in an primordial  $r^{-2}$  envelope. Panels (a) and (b): temperatures at 47.6 kyr and 135 kyr, respectively. Panels (c) and (d): densities at 47.6 kyr and 135 kyr, respectively.

### 3.1. $H/He$ Cooling in Ionized and Shocked Gas

$H_2$  was allowed to form but not cool the gas in the first run. As an experiment, we toggled the five atomic H and He cooling processes to determine their effect on the temperature of the ionized gas. We found (as expected) recombinational cooling to be dominant, reducing the postfront temperature from 60,000 K to 30,000 K. The remaining four channels collectively cooled the gas another 4000 K, down to 26,000 K. All five rates are shown in Fig. 2 at 100 Kyr in the ionized and shocked neutral gas. The I-front ends at 0.94 pc in the plot and the shocked shell extends to 1.19 pc. While collisional ionizations briefly surpass recombinations near the front, bremsstrahlung, interestingly, is the second most important cooling mode in most of the H II region, primarily due to the relatively large temperatures associated with He ionization. Collisional excitation of neutral hydrogen then follows collisional ionization in order of importance in the postfront gas, with Compton cooling as the least effective.

Bremsstrahlung and collisional ionization and excitation drop sharply in the shocked gas, leaving only Compton and recombinational cooling to operate in the low free electron fractions there. For the sake of comparison, we overlay the Dalgarno & McCray (1972)

cooling rates for an electron fraction of 0.01 used in Whalen & Norman (2007). Metal line cooling is eight orders of magnitude greater than recombinations or Compton scattering. Indeed, if no cooling cutoff whatsoever was employed with the metal lines they would quickly collapse the shocked gas to very dense cold shell whose final thickness is bounded from below only by numerical resolution. We note that the Compton component is highly dependent on redshift; had this simulation been performed at  $z = 35$ , inverse Compton scattering would have dominated recombinations in the postshock shell.

Recombinational and Compton cooling are so low in the shocked gas that they are inconsequential to its structure. The density and temperature profiles of the shell are indistinguishable from those of a nonradiating shock. Instability formation, except possibly those due to Rayleigh-Taylor perturbations, is extremely unlikely in these circumstances.

### 3.2. $H_2$ Cooling

In the second model H, He and molecular hydrogen cooling is included but not Lyman-Werner dissociation, so  $H_2$  forms freely in the outer layers of the front. In the third model we activate  $H_2$  photodissociation as described in § 2.  $H_2$  cooling rates, temperatures, densities,

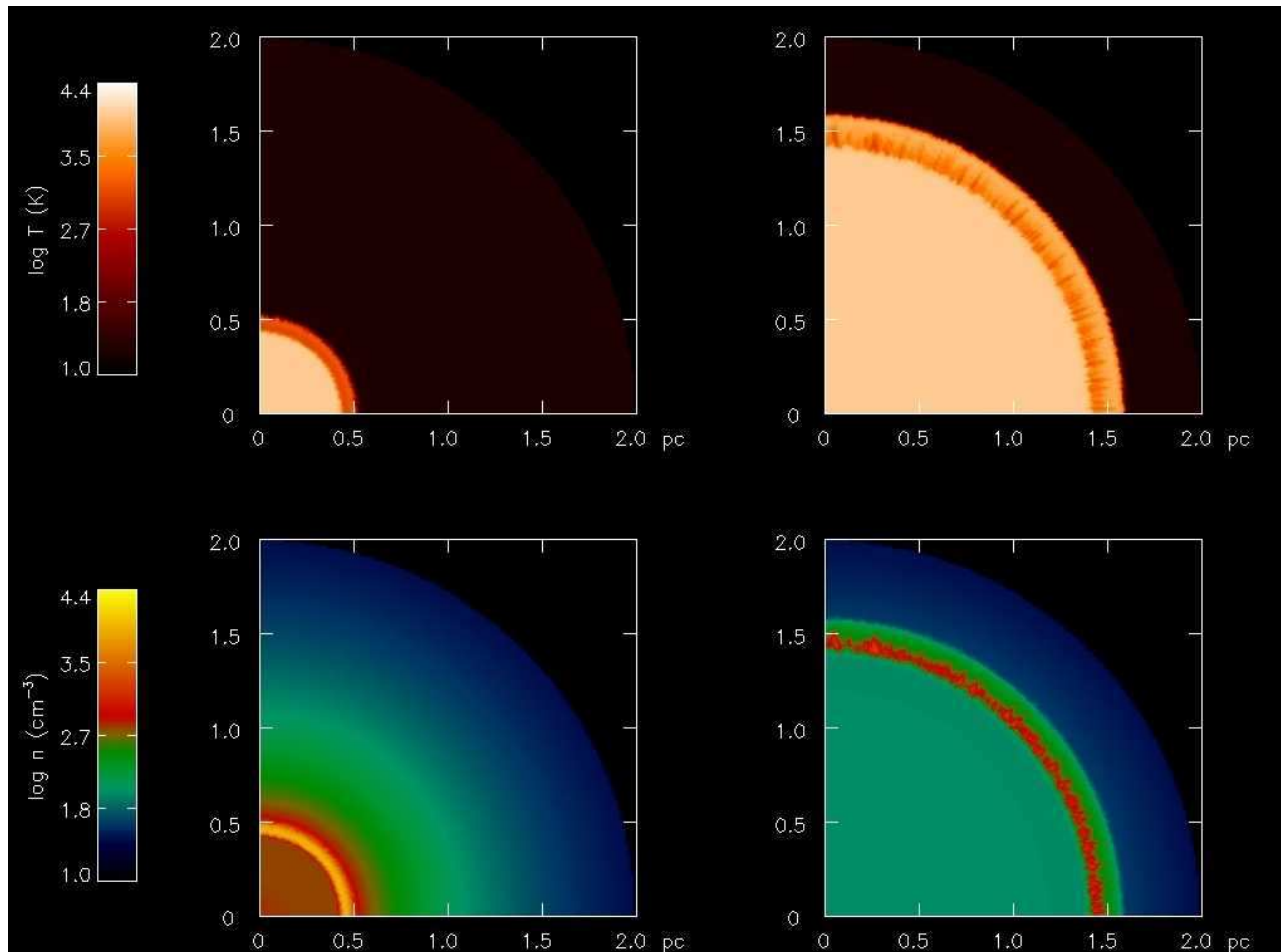


FIG. 4.— Evolution of a D-type front in an primordial  $r^{-2.7}$  envelope. Panels (a) and (b): temperatures at 47.6 kyr and 123.7 kyr, respectively. Panels (c) and (d): densities at 47.6 kyr and 123.7 kyr, respectively.

and velocities for both runs appear in Fig. 2. Molecular hydrogen efficiently drops the base of the shocked shell to 700 K in the absence of dissociating radiation, condensing the shell to higher peak densities than in the first set. It is likely in these circumstances that  $H_2$  cooling would cause unstable modes and shell breakup in primordial I-fronts.

However, at this proximity to the central star molecular hydrogen does not fully self-shield from the dissociating UV radiation, as shown in our third model. The sharp reduction in cooling rates attests to the efficiency with which LW photons destroy the  $H_2$  molecules (lowering their abundance by more than two orders of magnitude), resulting in a shell structure indistinguishable from one with atomic H cooling only. Comparison of the density profiles indicates that  $H_2$  cooling reduces the shell thickness by half in the absence of LW radiation and that it approaches the efficiency the Dalgarno & McCray curves within a thin layer at the base. The velocity profiles and positions of the two fronts indicates that  $H_2$  cooling slows the front by 10% in the absence of LW flux. Nevertheless, even with photodissociation the  $H_2$  cooling rates are comparable to the Dalgarno & McCray rates at electron fractions of 0.0001 - 0.001, suggesting that even low molecular hydrogen abundances set by LW fluxes may induce unstable modes in primordial I-fronts

(Whalen & Norman 2007), an issue to which we return below.

#### 4. DYNAMICAL INSTABILITIES IN D-TYPE PRIMORDIAL I-FRONTS

Can atomic cooling in H and He alone incite dynamical instabilities in D-type primordial ionization fronts? In this section we address both Vishniac and Rayleigh-Taylor instabilities driven by ionization fronts in perturbed spherically-symmetric density gradients.

##### 4.1. Vishniac Modes

Our one-dimensional model in § 3.1 revealed that I-front shocks cooled only by atomic H and He were indistinguishable from nonradiating shocks and therefore are not susceptible to Vishniac instabilities. To verify this prediction we performed a three-dimensional simulation with monoenergetic photons to prevent any complications due to multifrequency broadening of the front. In this run the same central photon rate, radial mesh and density profile were used as before but with 180 zones in theta and in phi, with reflecting boundaries at  $\pi/4$  and  $3\pi/4$  in both angles. The initial gas and cooling cutoff temperatures were set to the CMB background at  $z = 20$  and to 1000 K, respectively. The energy per ionization  $\epsilon_I$  was chosen to be 1.6 eV in order to set the postfront temperature to 10000 K. Thus, while He was present in

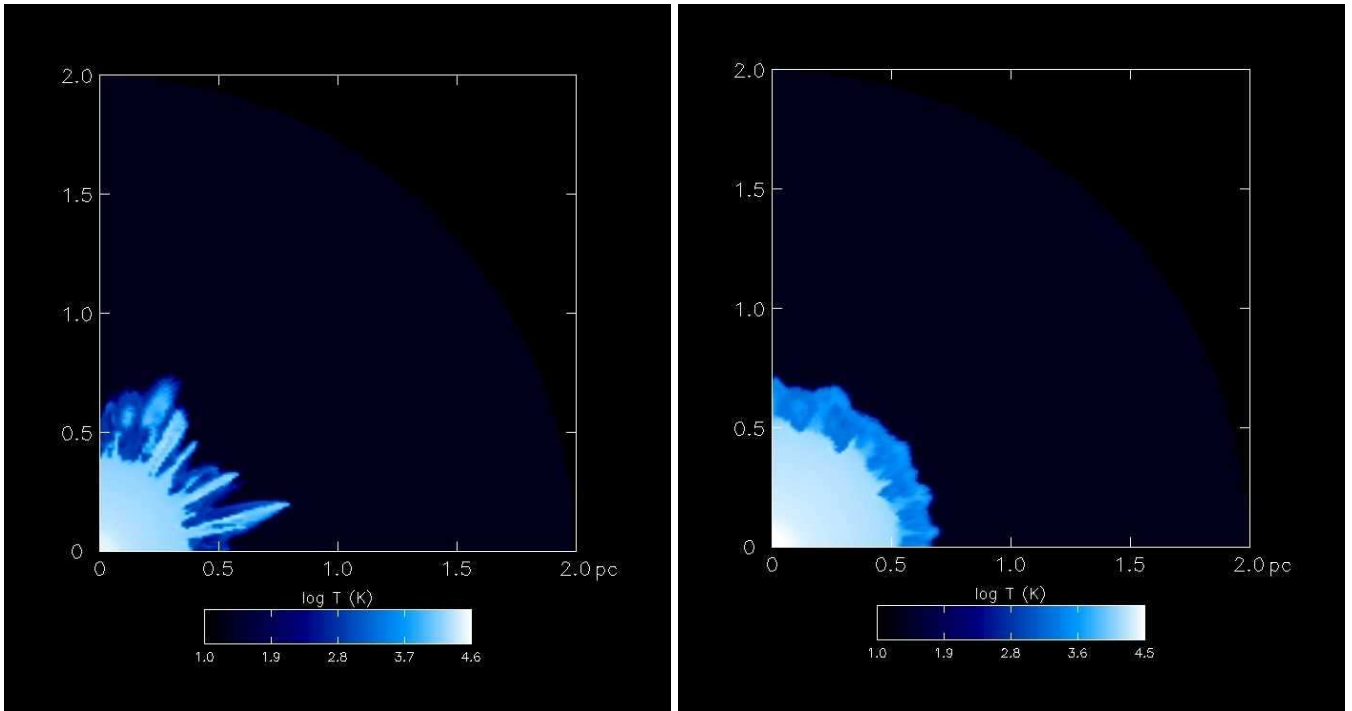


FIG. 5.— Temperature images of  $H_2$  mediated thin-shell instabilities in primordial ionization fronts. Left: no LW radiation, 40 kyr. Right: LW radiation included, 51.4 kyr.

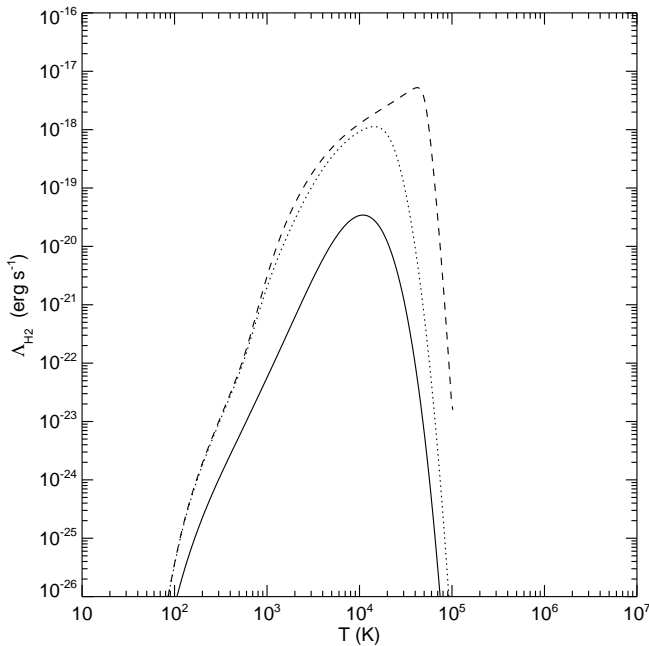


FIG. 6.— Galli & Palla (1998) molecular hydrogen cooling rates for three fiducial densities. Solid:  $n_{H_2} = 1 \times 10^2 \text{ cm}^{-3}$ ; dotted:  $n_{H_2} = 1 \times 10^4 \text{ cm}^{-3}$ ; dashed:  $n_{H_2} = 1 \times 10^8 \text{ cm}^{-3}$ .

the calculations to preserve its inertia to hydrodynamical motion, it was not ionized. Ignoring He ionization simply results in lower ionized gas temperatures, which do not deter instabilities from forming (He contributes even less to I-front shock cooling than H in these regimes).

To seed the formation of instabilities, we randomly varied the gas density of each cell by at most 1%, holding gas

energies constant to prevent pressure fluctuations from prematurely smoothing the perturbations. We only imposed these variations beyond radii of 0.125 pc to prevent the onset of shadowing instabilities in the R-type front before dynamical instabilities in the D-type front could form. In Fig. 3, the temperatures and densities reveal small fluctuations in the ionization and shock fronts due to the original perturbations, but they do not grow with time. The shell simply becomes thicker as more shocked neutral gas accumulates. We note the layer of gas photoevaporating into the interior of the H II region from the inner face of the shell in panel (a) of Fig. 3. It is visible as the thin red arc of lower densities bounding the yellow layer of denser shocked gas from below and can only be seen in the absence of instabilities. Our calculation confirms that dynamical instabilities in I-fronts cannot arise through the Vishniac instability in shocked gas cooled by only by H and He. Since our result depends only on cooling efficiencies, they will hold for the wide range of densities encountered in primordial halos and protogalaxies.

#### 4.2. Rayleigh-Taylor Modes

Rayleigh-Taylor (RT) instabilities can grow in primordial I-fronts if they accelerate in a density gradient, which is the case for profiles steeper than  $r^{-2}$ . We performed a run with parameters identical to those in § 4.1 except in a density gradient of  $r^{-2.7}$  and show  $\phi = \pi/4$  temperature and density slices of its evolution in Fig. 4. Perturbations in the dense shell are somewhat more pronounced than in the Vishniac run, hinting at the onset of unstable fingers, but they never fully materialize and disrupt the shock as the front exits the envelope. The shock clearly gains strength down the gradient, reaching temperatures of nearly 10,000 K. In such regimes electron-neutral collisions soon ionize the shock, helping the front to break



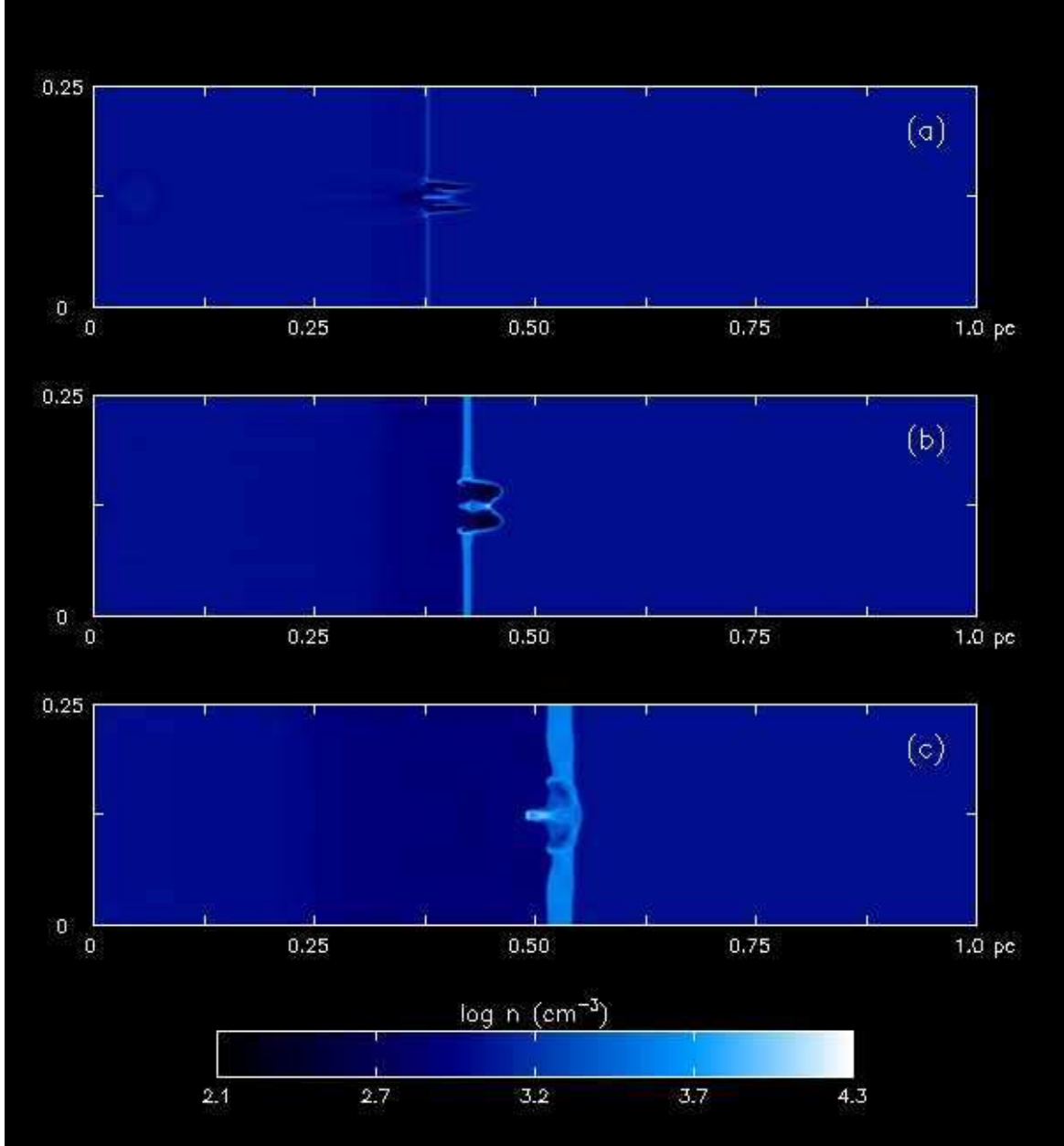


FIG. 7.— Density images of a shadow instability due to an underdense perturbation in atomic H with  $h\nu = 14.2$  eV and no  $\text{H}_2$  cooling: (a) 1.9 kyr, (b) 4.9 kyr, and (c) 12.6 kyr.

through. While possible in general, we find that RT instabilities fail to induce unstable modes in the front at these densities, which are typical of those in  $1 \times 10^5$  -  $1 \times 10^6 M_\odot$  minihalos at early epochs and of molecular cloud cores in protogalaxies at later times.

#### 4.3. Thin-Shell Modes Due to $\text{H}_2$ Cooling

We show in Fig. 5 the evolution of thin-shell instabilities in primordial D-type ionization fronts due to molecular hydrogen catalyzed at the base of the shocked shell. The first run was identical to that of § 4.1 except that  $\text{H}_2$  cooling was activated, but not LW photodissociation. The second was identical except Lyman-Werner flux was included. These models span the range of self-shielding anticipated in cosmological halos and protogalaxies, from virtually none to complete. In the absence of LW pho-

tons,  $\text{H}_2$  abundances of  $1 \times 10^{-3}$  to  $1 \times 10^{-2}$  form at the I-front/shock interface and, as shown in the left panel of Fig. 5, are as effective as metals at instigating dynamical instabilities in the D-type front (compare with Fig. 5 of Whalen & Norman (2007)). When LW flux is included, equilibrium  $\text{H}_2$  fractions in the shell fall to  $1 \times 10^{-6}$  to  $1 \times 10^{-5}$  but, surprisingly, strong instabilities persist despite the diminished cooling. The key to this phenomenon is the temperature dependence of the  $\text{H}_2$  cooling curves, shown in Fig. 6. From 300 K, the typical temperature of a star-forming cosmological minihalo, to 3000 K, the temperature of the shock in the primordial front,  $\text{H}_2$  cooling rates rise by three orders of magnitude, offsetting losses due to the photodissociation of the shell. We find that the instabilities are not as violent but still heavily perturb the shock.



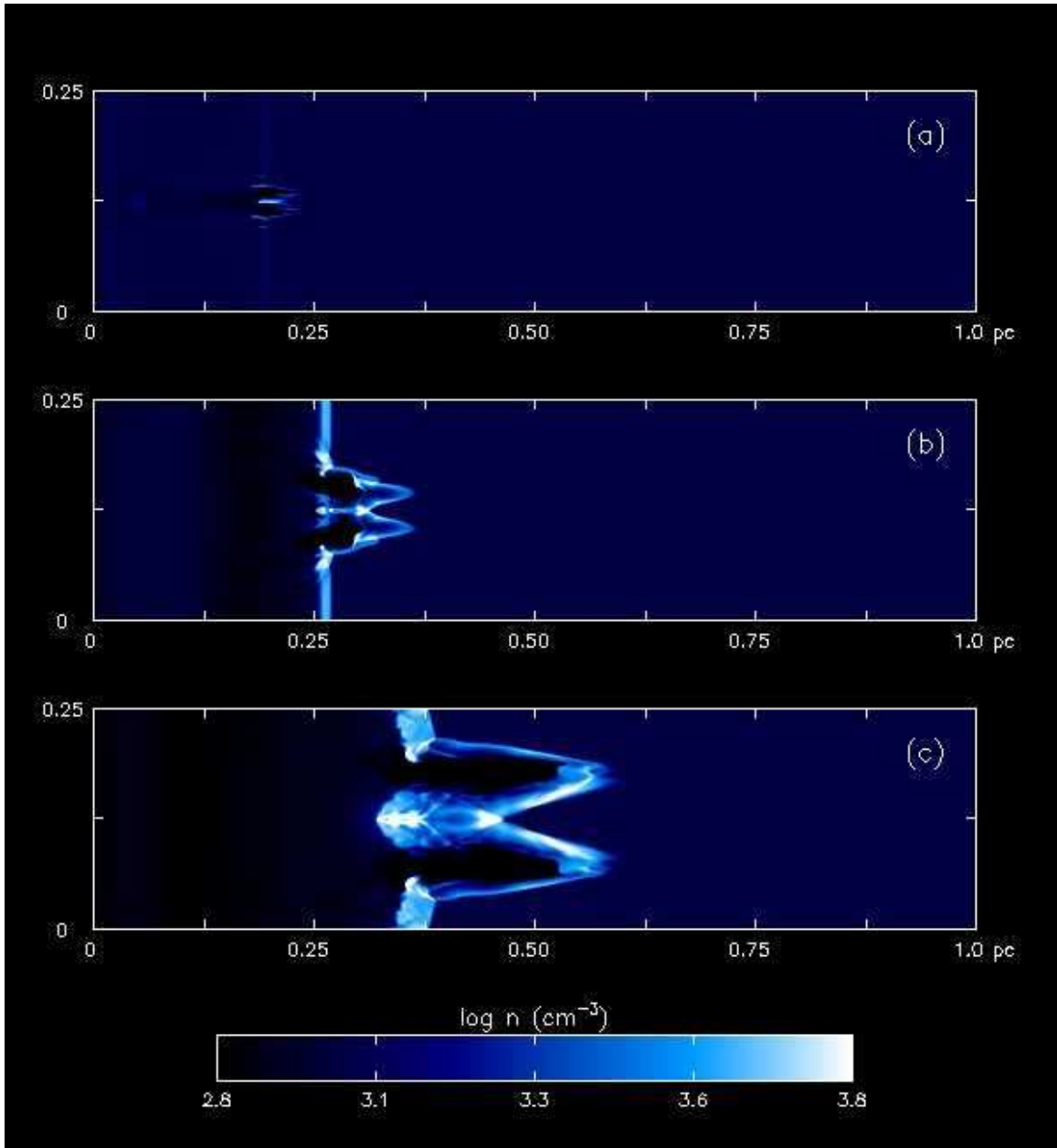


FIG. 8.— Shadow instability due to an underdense perturbation, full nine species primordial chemistry with a 100,000 K blackbody spectrum: (a) 1.3 kyr, (b) 6.3 kyr, and (c) 13.4 kyr.

Since our assumed central densities are lower than those in which Pop III stars form, we expect that  $\text{H}_2$  will be more heavily shielded and thin-shell instabilities will be more violent in primordial halos and protogalaxies than in this second case. Preliminary calculations in  $1 \times 10^6 M_\odot$  halo profiles hosting  $120 M_\odot$  stars confirm this suspicion, even with their much larger LW fluxes. These two cases likely bracket the magnitudes of the instabilities that occurred in primordial D-type ionization fronts.

##### 5. SHADOW INSTABILITIES IN R-TYPE PRIMORDIAL I-FRONTS

To test if the shadow instability can form in primordial, we performed a calculation in which a plane-parallel R-type ionization front enters the  $yz$ -face of a rectangular

box with a uniform density except for a spherical underdensity that is slightly offset from the face of entry. Its density decreases linearly in radius from the ambient value at its center to 50% below this amount at its surface. Our simulation mesh is 1.0 pc along the  $x$ -axis and 0.25 pc along the  $y$  and  $z$ -axes, with 1000, 250, and 250 zones in the  $x$ ,  $y$ , and  $z$  directions respectively. The gas density in the box is  $1000 \text{ cm}^{-3}$  with a temperature of 72 K to establish a sound speed  $c_s$  of 1 km/s. The incident photon flux along the  $x$ -axis at the face of entry is  $3.0 \times 10^{11} \text{ cm}^{-2} \text{ s}^{-1}$  to approximate that of a  $120 M_\odot$  star at 1.71 pc. The radius of the perturbation is 0.0125 pc and is placed 0.05 pc along the  $x$ -axis and centered in the  $yz$ -plane. Inflow and outflow boundary conditions were assigned to the 0 pc and 1.0 pc faces, respectively, with reflecting boundaries on the other four faces.

### 5.1. Monoenergetic Spectrum/Atomic Cooling

We first consider shadow instabilities in H gas with monoenergetic photons to avoid front broadening, with fixed energy per ionization  $\epsilon_I = 0.8$  eV to ensure post-front temperatures of 10000 K. We show xy density slices at  $z = 0$  of the instability in Fig. 7 at 1.9 kyr, 4.9 kyr, and 12.6 kyr. By 1.9 kyr the front has become D-type and the original corrugation in the R-type front is now non-linear. The expanding photoevaporated perturbation is faintly visible on the left in the figure. The double peaks are cross sections of a ringed jet whose morphology is due to the radial density profile of the sphere. The R-type front preferentially advances along lines of sight parallel to the x-axis that cut the underdense regions close to the surface of the sphere. Along the axis piercing the sphere through its center, the front advances at nearly the same rate as in the unperturbed medium because the densities along this path through the sphere are closer to those in the surrounding gas.

The evolution of the instability is qualitatively similar at first to that in Fig. 8 of Whalen & Norman (2007), but it quickly dampens and becomes subsumed in the inefficiently cooled shocked shell. The density knots in the shock located above and below the midplane of the jets at their base in the Whalen & Norman (2007) run are also visible in this run at first but they rapidly dissipate with little lateral migration across the face of the shock. If the assertion by Williams (1999) that these knots are odd-even numerical instabilities is true, they cannot survive long in the steadily thickening shocked layer at these densities. Rather than condensing and fragmenting, the shell tends to expand back into the jet, crowding its rarefied interior with gas that shields its tip from incident radiation and collapsing it back into the face of the shock. The collapse of the jet back into a dimple imparts considerable vorticity to the shocked gas in the vicinity of the disturbance, as is evident in panel (c). We find that atomic hydrogen cooling effectively quenches the shadow instability, but not before it significantly churns the face of the shock.

### 5.2. Blackbody Spectrum/ $H_2$ Cooling

The jet instability is far more violent when full nine-species primordial chemistry, the blackbody spectrum of the 100,000 K primordial star, and molecular hydrogen cooling are included, as we show in Fig. 8. Here, it is the higher post-front gas temperatures associated with multifrequency ionization of H and He that sustain and destabilize the jet. At 35,000 K, the high pressure of the ionized gas prevents the shocked shell ( $\sim 10,000$  K) from expanding and backfilling the rarefied jet, so the dimple never heals or collapses back into the face of the shock. The role of  $H_2$  cooling is minimal. The thickness of the shell in this model is indistinguishable from that with atomic cooling only, but the persistence of some molecular hydrogen likely promotes some small-scale fragmentation of the shell. We observe no saturation of the jet and it continues to grow with time. Maximum overdensities due to clumping of gas are approximately 10 in both runs.

## 6. METALLICITY THRESHOLD FOR D-TYPE INSTABILITY FORMATION

In § 4 it was shown that violent dynamical instabilities do not manifest in shocked shells cooled by atomic H only. At what metallicity do dynamical instabilities appear in D-type I-fronts in the absence of  $H_2$  cooling? We performed a grid of calculations with Dalgarno & McCray cooling in metallicities of  $1 \times 10^{-4} Z_\odot$ ,  $1 \times 10^{-3} Z_\odot$ ,  $1 \times 10^{-2} Z_\odot$ ,  $0.1 Z_\odot$ , and  $1.0 Z_\odot$  to ascertain if there is threshold to instability growth. The problem setup is the same as in the three-dimensional  $r^{-2}$  run described in § 4.1, again assuming an initial electron fraction of  $1 \times 10^{-4}$  appropriate for  $z \sim 20$ . At such low fractions the cooling in the gas is chiefly due to excitation of metals by collisions with neutral hydrogen (see Fig. 2 in Dalgarno & McCray (1972)). At solar metallicity these cooling rates lie approximately an order of magnitude below the Dalgarno & McCray curve shown in Fig. 2. Our metallicities were chosen to survey cooling efficiencies between the very low purely atomic rates and quite large  $1 Z_\odot$  metal line curve. We apply a cooling cutoff temperature of 1000 K rather than the CMB temperature. This limits the thickness to which the shell can collapse so the metallicity at which instabilities appear is truly the threshold for their formation.

In Fig. 9 the I-front and shock are shown at 125.5 kyr for our six choices of metallicity. We include in panel (a) the front in a zero-metallicity gas as a reference case in which no unstable modes arise. Noticeable perturbations appear in the front in roughly equal numbers in gas enriched to  $1 \times 10^{-4} Z_\odot$  and  $1 \times 10^{-3} Z_\odot$  (panels (b) and (c), respectively); those in panel (c) are slightly more pronounced but in neither case do they grow significantly with time or penetrate the shell to disrupt the shock. The agitation in the front does perturb the shock in the  $1 \times 10^{-2} Z_\odot$  gas, with visible hydrodynamical motions above and below the image plane. Also, consolidation of initially short-wavelength modes into fewer larger-wavelength structures is evident, clearly demonstrating the evolution in D-type fronts predicted by Giuliani (1979). These features are even more pronounced in the  $0.1 Z_\odot$  case, and the instability completely deforms the shock in the  $1.0 Z_\odot$  gas.

If one adopts deformation of the shock and wavelength evolution of the unstable modes as the criteria for instability formation, it appears that metallicities of  $\sim 1 \times 10^{-2} Z_\odot$  are the threshold for perturbation growth in these densities. However, we note that primordial gas in relic H II regions would be susceptible to ionization front instabilities at considerably lower metallicities because they are compensated by larger free electron abundances. Our results indicate that this type of flow instability would operate even in marginally enriched protogalaxies and star-forming minihalos. The morphology of the instabilities at later times suggest that they might be efficient at driving turbulence in the shock, which could have important implications for the time scales of subsequent star formation in the region (Whalen & Norman 2007). Finally, we note that instabilities readily erupt at solar metallicities even with the much lower initial electron fraction  $\chi_e$  of 0.0001 than the  $\chi_e = 0.01$  value adopted in Whalen & Norman (2007). While in general it is difficult to know what free electron abundances are present in a galactic molecular cloud, a reasonable assumption is that all the carbon in the gas is singly ionized by the UV background. This yields a lower bound

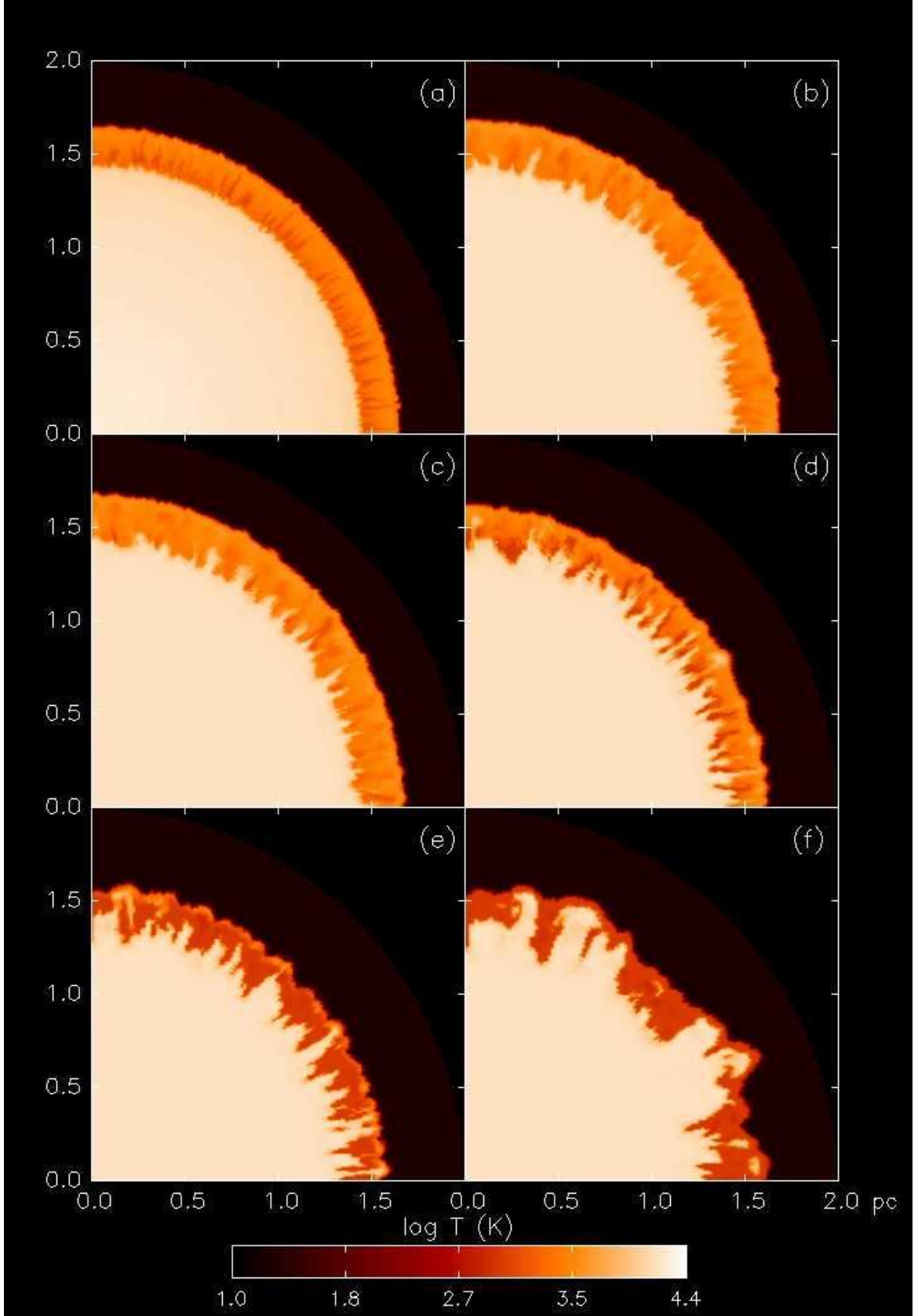


FIG. 9.— Dynamical instability in an  $r^{-2}$  density gradient in a variety of metallicities at 125.5 kyr. Panel (a): zero metallicity. Panels (b), (c), and (d) are for metallicities of  $1 \times 10^{-4} Z_{\odot}$ ,  $1 \times 10^{-3} Z_{\odot}$ , and  $1 \times 10^{-2} Z_{\odot}$ , respectively, while panels (e) and (f) are for  $0.1 Z_{\odot}$  and  $1.0 Z_{\odot}$ , respectively.

for electron fractions in star forming regions in the galaxy today that is on the order of those applied in this grid of metallicities, confirming that I-front instabilities will be a general feature of those regions.

## 7. DISCUSSION AND CONCLUSIONS

Instabilities readily form in primordial ionization fronts, even in the absence of metals. However, they emerge only when calculations couple multifrequency radiative transfer to gas phase primordial chemistry, which is crucial to capturing the formation of  $H_2$  that triggers dynamical instabilities in self-shielded shells or the high post-front gas temperatures that perpetuate shadow instabilities. We find that thin-shell modes cannot develop in atomic H and He but that Rayleigh-Taylor instabilities are not ruled out. Nevertheless, they do not appear on the time scales of UV breakout from the density profiles in our models, which roughly approximate those in cosmological halos.

Dynamical instabilities in D-type fronts were probably common in centrally-concentrated structures capable of molecular hydrogen self-shielding, like cosmological minihalos at subparsec radii and molecular cores in primitive galaxies. However, shadow instabilities appearing earlier in R-type fronts and needing no  $H_2$  cooling may have pre-empted thin-shell instabilities in more evolved I-fronts. Inhomogeneities endemic to all primordial structures made this instability ubiquitous, forming shocks and clumps that regulated the escape of ionizing UV photons and metals from the first luminous objects.

One question that remains to be answered is how instabilities forming at subparsec radii deep in cosmological halos or early galaxies governed the final morphologies of H II regions on kiloparsec scales. If clumping due to unstable modes was long-lived, UV breakout along adjacent lines of sight may have been significantly delayed, causing the formation of extended fingers of ionized gas into the early IGM that resulted in serious departures from the classical “butterfly” appearance of many cosmological H II regions (Abel et al. 2006). Numerical models bridging the spatial scales between the young D-type front and final H II region are now under development.

Ionization front instabilities in the accretion envelopes of the first stars may have allowed them to grow to much larger masses than predicted by analytical models of infall reversal (Tan & McKee 2004). Fingers of ionized gas elongating outward through the accretion shock might have channelled ionizing radiation out of the cloud that would otherwise have staunched infall. Accretion could then continue downward in columns of neutral flow, allowing the star to bypass the final mass limits set by the cutoff models.

The strength and longevity of I-front instabilities determined their impact on subsequent star formation.

Prominent extrusions from the front out into the halo or host galaxy might have created clumps of primordial gas prone to gravitational collapse by HD cooling in the relic H II region, forming a new generation of stars without recourse to chemical enrichment. This scenario merits further study with high resolution methods, as it is uncertain if clumps could have collapsed outside the potential well of the dark matter halo. On the other hand, more saturated modes due to less efficient cooling and fragmentation of the shell may instead have provided turbulent support against condensation in larger cloud complexes within protogalaxies, suppressing rather than promoting star formation.

Clumping by instabilities may have determined the extent of the first metal bubbles (Johnson et al. 2007) in addition to modulating UV escape fractions and the final radii of H II regions. Mixing of metals with clumps may also have accelerated second generation star formation. Efficiently cooled clumps would have collapsed to form stars on mass scales very different from their predecessors. Accurate models of primordial H II regions that include ionization front instabilities will establish the proper initial conditions for metal mixing in the next generation of early chemical enrichment studies.

Although dynamical instabilities due to heavier elements appeared at metallicities of 0.001 - 0.01 at ionized fractions of 0.01, they would have appeared in abundances an order of magnitude lower in the higher free electron fractions of fossil H II regions. This is comparable to the metallicity associated with the transition from Pop III stars to less massive populations (Mackey et al. 2003); hence, instability formation, and its consequences, smoothly followed rollovers in initial mass functions (IMFs) in the early universe.

We neglect direct transport of recombination photons, which may limit the growth of unstable modes. Reprocessed radiation emanating from within ionized extensions of gas may erode the sides of the fingers, photoevaporating overdensities in the troughs. This may not be an important effect in shadow instabilities since the interior of the jet is relatively rarefied, with low recombination emissivities.

DW thanks Tom Abel, Kyungjin Ahn and Alex Heger for helpful discussions concerning these simulations and we thank the anonymous referee whose comments improved the quality of this paper. This work was carried out under the auspices of the National Nuclear Security Administration of the U.S. Department of Energy at Los Alamos National Laboratory under Contract No. DE-AC52-06NA25396. The simulations were performed at SDSC and NCSA under NRAC allocation MCA98N020.

## REFERENCES

- Abel, T., Anninos, P., Zhang, Y., & Norman, M. L. 1997, *New Astronomy*, 2, 181
- Abel, T., Bryan, G. L., & Norman, M. L. 2000, *ApJ*, 540, 39
- Abel, T., Bryan, G. L., & Norman, M. L. 2002, *Science*, 295, 93
- Abel, T., Wise, J. H., & Bryan, G. L. 2006, *astro-ph/0606019*
- Ahn, K., & Shapiro, P. R. 2007, *MNRAS*, 375, 881
- Alvarez, M. A., Bromm, V., & Shapiro, P. R. 2006, *ApJ*, 639, 621
- Anninos, P., Zhang, Y., Abel, T., & Norman, M. L. 1997, *New Astronomy*, 2, 209
- Bromm, V., Coppi, P. S., & Larson, R. B. 1999, *ApJ*, 527, L5
- Bromm, V., Coppi, P. S., & Larson, R. B. 2002, *ApJ*, 564, 23
- Dalgarno, A. & McCray, R. A. 1972, *ARA&A*, 10, 375
- Draine, B. T., & Bertoldi, F. 1996, *ApJ*, 468, 269
- Franco, J., Diaz-Miller, R. L., Freyer, T., & Garcia-Segura, C. 1998, *ASP Conf. Ser. 141: Astrophysics From Antarctica*, 141, 154
- Fuller, T. M. & Couchman, H. M. P. 2000, *ApJ*, 544, 6
- Galli, D., & Palla, F. 1998, *A&A*, 335, 403
- Garcia-Segura, G., & Franco, J. 1996, *ApJ*, 469, 171

- Giuliani, J. L. 1979, *ApJ*, 233, 280
- Johnson, J. L., Greif, T. H., & Bromm, V. 2007, *ApJ*, 665, 85
- Kitayama, T., Yoshida, N., Susa, H., & Umemura, M. 2004, *ApJ*, 613, 631
- Kogut, A. et al. 2003, *ApJS*, 148, 161
- Mac Low, M.-M., & Norman, M. L. 1993, *ApJ*, 407, 207
- Mackey, J., Bromm, V., & Hernquist, L. 2003, *ApJ*, 586, 1
- Mizuta, A., Kane, J. O., Pound, M. W., Remington, B. A., Ryutov, D. D., & Takabe, H. 2005, *ApJ*, 621, 803
- Mizuta, A., Kane, J. O., Pound, M. W., Remington, B. A., Ryutov, D. D., & Takabe, H. 2006, *ApJ*, 647, 1151
- Osterbrock, D. *Astrophysics of Gaseous Nebulae and Active Galactic Nuclei*, University Science Books 1989.
- Page, L., et al. 2006, *astro-ph/0603450*
- Ricotti, M., Gnedin, N. Y., & Shull, J. M. 2001, *ApJ*, 560, 580
- Schaerer, D. 2002, *A&A*, 382, 28
- Shapiro, P. R., & Kang, H. 1987, *ApJ*, 318, 32
- Spergel, D. N. et al. 2003, *ApJS*, 148, 175
- Tan, J. C., & McKee, C. F. 2004, *ApJ*, 603, 383
- Vishniac, E. T. 1983, *ApJ*, 274, 152
- Whalen, D., Abel, T., & Norman, M. L. 2004, *ApJ*, 610, 14
- Whalen, D., & Norman, M. L. 2006, *ApJS*, 162, 281
- Whalen, D., & Norman, M. L., *astro-ph/0703463*.
- Williams, R. J. R. 1999, *MNRAS*, 310, 789
- Yoshida, N., Abel, T., Hernquist, L., & Sugiyama, N. 2003, *ApJ*, 592, 645
- Yoshida, N., Oh, S. P., Kitayama, T., & Hernquist, L. 2007, *ApJ*, 663, 687